Distribution of broad plasma depletions in the equatorial F region observed by the C/NOFS satellite

Jong-Min Choi[1,2], Young-Sil Kwak[2,3*], Hyosub Kil[4], Jaeheung Park[2,3], Woo Kyoung Lee[2], Yong-Ha Kim[5], and Junseok Hong[2,5]

[1]Department of Earth Sciences, National Cheng Kung University, Tainan, Taiwan

[2]Space Science Division, Korea Astronomy and Space Science Institute, Daejeon, South Korea

[3]Department of Astronomy and Space Science, Korea University of Science and Technology, Daejeon, South Korea

[4]The Johns Hopkins University Applied Physics Laboratory, Laurel, Maryland, USA

[5]Department of Astronomy and Space Science, Chungnam National University, Daejeon, South Korea

---

(*) Corresponding author: Young-Sil Kwak (e-mail: yskwak@kasi.re.kr)

Short title: DISTRIBUTION OF BROAD PLASMA DEPLETIONS

Three main points:

1. BPDs occur predominantly at postmidnight in comparison to premidnight.
2. BPDs occur more frequently during periods of low solar activity and during the June solstices.
3. Generation of BPDs is associated with lower scale height, stagnant background plasma and storm-time disturbance dynamo.

Abstract

Broad plasma depletions (BPDs) are bubble-like plasma depletions in the equatorial F region whose longitudinal widths (> 4 degree) are greater than those of regular bubbles. Their occurrence in satellite observations is understood in terms of the uplift of the ionosphere; BPDs are observed when satellites pass through the bottomside of bubbles. However, a merger of bubbles is also suggested as the cause of BPDs. We investigate the origin of BPDs by examining the occurrence climatology of BPDs and its association with vertical plasma motion. Our preliminary results derived from the C/NOFS observations in 2008–2012 show that BPDs occur more frequently during lower solar activity, during higher magnetic activity, and at lower altitudes. BPDs during solar maximum and minimum periods show different behavior. BPDs during solar maximum period occur frequently at premidnight and during the equinoxes and December solstices (for highly geomagnetically disturbed periods). On the contrary, BPDs during the solar minimum period occur predominantly at postmidnight and during the June solstices. The occurrence rates of postmidnight BPDs are positively correlated with AE index and are inversely correlated with 10.7 cm solar radio flux. Low solar activity creates favorable conditions for generating BPDs by thinning the F region. At the solar minimum, the density of the F region's bottomside changes significantly even with slight altitude shifts, which can be recognized as BPDs. When a geomagnetic disturbance occurs, the eastward electric field can be enhanced at the equatorial F region, and the entire F layer can move upward.

1. Introduction

The plasma depletions in the equatorial F region have various sizes of irregularities during the nighttime. A typical phenomenon of irregularities, bubbles, has formation of deep plasma density depletion structures over a narrow longitude and latitude. Sometimes, especially when there is a geomagnetic disturbance, plasma depletion is formed over a wider space, which is called a broad plasma depletion (BPDs). BPDs in the equatorial F region are plasma depletions over several hundred kilometers in longitude and latitude.

BPDs were mainly found from in-situ satellite observations during geomagnetic disturbance: the Defense Meteorological Satellite Program (DMSP) at 840 km altitude (Basu et al., 2007; Burke et al., 2000; Greenspan et al., 1991; Kil & Paxton, 2006; Kil et al., 2006), the first Republic of China Satellite (ROCSAT-1) at 600 km altitude (Su et al., 2002), the Korea Multipurpose Satellite-1 (KOMPSAT-1) at 685 km altitude (Lee et al., 2002), and the Communication/Navigation Outage Forecasting System (C/NOFS) from 400 km to 850 km altitude (Burke et al., 2009; Huang et al., 2009; Huang et al., 2011, 2012; Kil & Lee, 2013; Kil et al., 2014, 2016; Lee et al., 2014).

There are two hypotheses regarding the mechanism of BPDs; merging bubbles and ionospheric uplift. Merging process is responsible for the BPDs observed near plasma bubbles. Plasma bubbles grow and merge to form BPDs (Huang et al., 2011, 2012; Kil & Paxton, 2006; Kil et al., 2006). However, some BPDs are observed without any signature of plasma bubbles (Kil & Lee, 2013, Kil et al., 2014, 2016; Lee et al., 2014). In other words, BPDs are found in longitudinal regions where C/NOFS did not detect bubbles before BPDs detection. As such, Kil et al. (2013) claimed that bubbles are not a necessary condition for BPDs formation.

According to the second hypothesis, the cause of BPDs is a geomagnetic disturbance, which

introduces an electric field to the low-latitude ionosphere. The enhanced eastward electric field moves the plasma upward via the E × B drift. BPDs are detected when the satellites pass through the upwelling edge at F region bottomside during geomagnetic disturbance time. Therefore, a large and wide density depletion has been observed as the satellite observes the region.

The goal of this study is to identify the characteristics of BPD occurrence rate and to check the mechanism of BPD generation. For this purpose, we use the measurements of the plasma density taken by the Planar Langmuir Probe (PLP) on board the C/NOFS satellite. The C/NOFS satellite was launched in April 2008 into an elliptical orbit at an altitude of 400 km-850 km. Its orbital inclination was 13°.

Though a number of studies have investigated the characteristics of BPDs extensively, there is still room for further improvement. Since DMSP and KOMPSAT-1 are on sun-synchronous orbits, the ionosphere can only be monitored at a limited range of local time. The ROCSAT-1 has a circular orbit, and its altitude was fixed at 600 km. The operating period of KOMPSAT-1 and ROCSAT-1 is near the peak of solar activity. On the other hand, since C/NOFS has an elliptical orbit, the equator can be observed at various local time regions. In addition, since the altitude orbit is 400 km to 850 km and operating period is from solar minimum to moderate period, the BPD characteristics can be analyzed at various altitudes and solar activities.

Furthermore, most of the previous studies have explained the phenomenon with a few examples. We went one step further to find the BPDs automatically and checked their statistical characteristics. The data and methodology are explained in section 2. The results from statistical analysis of the BPDs are shown in section 3. In section 4, we discuss why the rate of BPDs occurrence is high under certain conditions. A conclusion for this study is given in section 5.

2. Data and methodology

The C/NOFS satellite was in an elliptical orbit (altitude: 400 km-850 km) with an orbital inclination of 13 degrees and launched on 16 April 2008. The low-inclination orbit assists in monitoring the ionosphere at all local time sectors. PLP on board the C/NOFS satellite detected the plasma density and temperature in situ. The data sampling rate of PLP is 512 Hz, and allows for detection of irregularities as small as 13 m. In this study, we analyze the plasma density measurements using 1s average data, because the BPDs structure forms over several hundred kilometers.

To illustrate the methodology used to automatically detect BPDs, we used BPDs observed on 11 December 2010 as an example. The black curve in Figure 1a shows in situ measurements of the plasma density obtained from the PLP data. The red curve indicates the background density. The background density is determined by repeated smoothing and removal of the low density region. The observed density was smoothed using 50 data points. Then, the background density is obtained by repeating the smoothing operation 5 times based on the assumption that the variation of background density is smooth with respect to longitude.

Figure 1b represents the difference between the logarithm of the plasma density (N_i) and logarithm of the background density (N_0). Figure 1c shows the absolute values of the results in Figure 1b. The red dashed line in Figure 1c is the threshold value ($\sigma > 0.2\,\%$), which is used to remove very small density perturbations. The equatorial ionization trough, which shows a gradual density variation, is not included. The data points exceeding the threshold value in Figure 1c are given as Flag 1, and those that do not exceed the threshold value are treated as Flag 0, and the result is shown in Figure 1d. Since we focus on irregularities over several hundred kilometers in longitude and latitude, we have assumed that values above the threshold must be

maintained over at least 60 consecutive data points (4 degrees) for longitude. The BPDs based on that assumption are shown in Figure 1e.

3. Results

Figure 2a shows the local time distribution of the occurrence of BPDs during 2008-2012. After the BPDs were automatically detected, various parameters corresponding to the median UT values of each of the BPDs were used for statistical analysis. BPDs are detected automatically from the PLP data orbit according to orbit. We processed the PLP data from 2008-2012. The total number of BPDs is 378. There are 53 premidnight BPD events and 325 postmidnight BPD events.

BPDs are observed after 18:00 LT and have a peak occurrence rate between 02:00 and 04:00 LT. Although BPDs were found at premidnight in previous case studies, our statistical analysis shows that BPDs occur predominantly postmidnight. A number of researchers have used DMSP and KOMPSAT-1 satellite data to study BPDs occurring before midnight due to the Sun-synchronous satellite orbit (Basu et al., 2007; Burke et al., 2000; Greenspan et al., 1991; Kil & Paxton, 2006; Kil et al., 2006, Lee et al., 2002). In ROCSAT-1 and C/NOFS satellite data, BPDs are also observed after midnight (Burke et al., 2009; Huang et al., 2009; Huang et al., 2011, 2012; Kil & Lee, 2013; Kil et al., 2014, 2016; Lee et al., 2002; Lee et al., 2014, Su et al., 2002). In the following discussions, we categorize BPDs into two groups separated by the local midnight, because we can identify different mechanisms depending on the local time.

Figure 2b shows the magnetic latitude distribution of BPDs occurrence. BPDs are frequently observed around the magnetic equator within ±5° magnetic latitude, regardless of the classification of pre-/post-midnight BPDs. These results indicate that BPDs are not a

136 phenomenon that occur at other latitudes, but near the magnetic equator.

137 Figure 2c shows the occurrence rate of BPDs as a function of Kp. The occurrence rates were
138 presented in the form of a percentage (%) with respect to the total data points during 2008-2012.
139 C/NOFS PLP data are not distributed equally for different Kp values. Therefore, the actual
140 number of BPD occurrences can be biased by the uneven data distribution. As such, the
141 occurrence rate is considered to identify the distribution as function of Kp. The occurrence rates
142 of BPDs show an increasing trend with an increase of Kp. Although the number of premidnight
143 BPDs is very small compared to postmidnight, premidnight BPDs appear primarily in Kp
144 between 6 and 7. This means that premidnight BPDs mainly occur when there is a strong
145 geomagnetic disturbance.

146 BPDs are mostly observed at lower apex altitudes in Figure 2d. According to the BPD
147 formation mechanism suggested by Kil et al. (2014), more BPDs are expected on the F region
148 bottomside because BPDs are nothing but the uplifted bottomside of the F region. This
149 phenomenon can be confirmed in the high-resolution plasma bubble model of Yokoyama et al.
150 (2014), where the F region bottomside bubble more closely resembles BPDs than the F region
151 topside bubble. On the contrary, according to the merging bubble mechanism identified by
152 Huang et al. (2011), more BPDs must be observed at the topside, because the bubble grows
153 vertically and then merges. Therefore, our Figure 2d seems to support Kil et al. (2014), who
154 interpreted BPDs as updraft of F region bottomside.

155 Figure 3 shows the monthly distribution of the occurrence rate of BPDs for five years. BPD
156 occurrences clearly peak at solar minimum. Significantly, most of them are observed in June,
157 while the secondary occurrence maximum occurs in December. According to the uplift
158 mechanism (Kil & Lee, 2013; Kil et al., 2014, 2016; Lee et al., 2014), when the entire F region is

lifted up and the satellite passes below it, it is considered as a BPD. Nishioka et al. (2012) also presented that the post-midnight field-aligned irregularities by 30.8 MHz radar and the uplift of the F layer represented by hmF2 were frequently seen around midnight during a solar minimum period between May and August at Kototabang, Indonesia. Figure 3 indicates that the increasing 10.7 cm solar radio flux decreases the occurrence of BPDs. When a large number of BPDs are observed, the AE index is relatively high. This is consistent with the explanation that the eastward electric field caused by the geomagnetic activity increases in the equatorial F region around BPDs.

In Figure 4, the distributions of the rate of occurrence of BPDs are shown for three seasons: June solstice (May, June, July, and August), December solstice (November, December, January, and February), and Equinox (March, April, September, and October). Then, BPDs are divided into two groups based on the local time. The green curves represent premidnight BPDs, while blue curves indicate postmidnight ones. The 10.7 cm solar radio flux during 2008-2012 is shown with red curves. The rate of occurrence of BPDs tends to decrease with increasing solar activity. BPDs occur more frequently during the period of low solar activity and during the June solstices. This tendency is most prominent in postmidnight BPDs. Seasonally, the negative correlation with solar activity is clearly visible around the June solstice. On the other hand, in December and equinox, the correlation seems weak, albeit certainly negative.

4. Discussion

4.1. Postmidnight BPDs during low solar activity

In this paper, we report the characteristics of the apex height, K_p index, day of year, seasonal and solar activity effects on the equatorial BPDs. Based on the occurrence climatology,

BPDs observed by C/NOFS can be characterized as the phenomena at postmidnight, near the magnetic equator, at the lower part of the ionospheric F-region, during solar minimum, and during the June solstice. In particular, postmidnight BPDs are strongly dependent on the solar activity (i.e., occurrence rate of postmidnight BPDs is higher for low solar activity) and occur frequently in June solstice. This solar activity dependence of BPDs occurrence can be related to scale height variations in the ionosphere.

In a plasma moving in the vertical direction, the plasma density changes according to the ionospheric thickness, and the change can be expressed by the scale height. The variation of ionospheric electron density at two altitudes (Δn_e) is associated with the height variation (Δh) in the F region bottomside and scale height (H_m) [Hargreaves, 1992].

$$\Delta n_e \propto exp\left(\frac{\Delta h}{H_m}\right)$$

H_m is a variable influenced by local time, season, and longitude. A low scale height means that density difference between the two altitudes is large – that is, the F region has contracted in its vertical extent. Δh, change of observation altitudes with respect to the F-region peak, is a variable that can be affected by the geomagnetic disturbance. In the equatorial ionosphere, Δh is known to change due to the disturbance-induced electric field.

The scale height is known to be related to the bottomside profile thickness. Lee & Reinisch (2007) investigated the scale height near the F region peak measured by digisonde at Jicamarca Radio Observatory (JRO) (11.95°S, 76.87°W) in Peru. Bottomside profile thickness is highly correlated with F_2 layer Chapman scale height (H_m). Liu et al. (2012) reported the variation of

thickness measured by Jicamarca digisonde during the last two solar minima: 1996-1997 and 2008-2009. At the geomagnetic equatorial station at Jicamarca, the thickness is lowest in June solstice 2008-2009, with very low solar activity. Liu et al. (2006) investigated the scale height of the F region peak using an ionogram. They showed that the F10.7 index shows an increasing trend with an increase of scale height around the F region peak height. At the solar minimum, the altitude extent of the F region peak becomes smaller than during the solar moderate periods because the scale height becomes smaller. Statistically, the most observed period for postmidnight BPDs is low solar activity and June solstice, where F region is known to contract most significantly. Under such conditions, the ionospheric density changes significantly, even for slight altitude changes. As such, low solar activity and June period make a good environment for postmidnight BPDs to occur.

For both mechanisms suggested for BPD generation, the uplift of the ionosphere and a merger of bubbles, updraft of the ionosphere should generate favorable conditions for BPD occurrence. In general, the vertical motion of the background plasma is upward during the daytime and downward during the nighttime. The upward drift peaks at about 18LT by prereversal enhancement, and the downward drift has a maximum at about 21LT. The amplitude of the vertical drift varies with the season, and the amplitude also varies with the solar flux (Fejer et al., 1991; 1995). While the amplitude of the vertical drift increases as the solar flux increases, in a low solar flux the amplitude of the vertical drift is small. In lower solar activity, the amplitude of average vertical plasma drifts measured at Jicamarca is very weak (Fejer et al., 1991). Particularly after midnight in the June solstice during low solar activity, background plasma drift is almost stagnant. Figure 5 shows vertical plasma drifts measured by incoherent scatter radar at JRO during three seasons for solar minimum (2008-2009) and solar moderate

(2011-2012) periods. During the solar minimum, the ionospheric plasma in June solstice has an upward motion after midnight, unlike other seasons. In the solar moderate period, plasma in all seasons did not drift upward after midnight, but an upward drift appeared in December solstice and equinox around 19 LT. In Figure 3, postmidnight BPDs are frequently observed during June solstice in 2008-2009, while the premidnight BPDs in 2011-2012 occur in December solstice and equinox: the BPD occurrence generally follows the season and solar activity dependence of the vertical drift of the background plasma. The background upward motion, which depends on season and solar activity, is an important factor in BPD generation.

The vertical plasma drift measured by C/NOFS Coupled Ion-Neutral Dynamics Investigation (CINDI) also showed that the vertical drift of the background plasma is weakly downward at midnight during low solar activity, but plasma depletion at sunset is rising slowly, so bubbles are observed at midnight (Smith et al., 2018). In addition, Stoneback et al. (2011) reported that the average vertical drifts are mostly downward in May, June, July, and August between 17:00 and 20:00 LT. As the vertical plasma drift is relatively less downward at postmidnight of June solstice during solar minimum, there is more opportunity for the satellite to observe the BPDs.

Let us assume a disturbance-induced electric field of the same magnitude at the solar minimum and solar maximum. As the electric field uplifts the equatorial F region, ionospheric density at a fixed altitude changes more rapidly at the solar minimum than at the solar maximum. Two factors are known to change the electric field in the equatorial ionosphere by geomagnetic disturbance. The first is the penetration electric field generated by the sudden changes in the solar wind and magnetosphere, which is generally short-lived (for a few hours at most). The other is the disturbance dynamo electric field caused by the neutral wind, the effect of which can

last longer than several hours. Blanc & Richmond (1980) presented a theory called disturbance dynamo. According to this theory, during a magnetic storm, energy is deposited into both polar regions and Joule heating occurs. The concomitant changes in the global wind circulation can induce a westward electric field in dayside and an eastward electric field in the nightside. After midnight, which is the focus of this study, the eastward electric field is induced in the equatorial ionosphere by the effect of disturbance dynamo electric field during the magnetic storm, and the ionosphere plasma is lifted.

In June solstice during low solar activity the F region has a small scale height and near-stagnant vertical drifts, which provides a good environment for the growth of BPDs. Under these conditions, the plasma density can change suddenly even at a slight altitude variation because the altitude slop of the plasma density becomes steep. On top of this pre-conditioning the disturbance-induced electric field in the background can lift up the ionosphere, leading to post-midnight BPDs in June at very low solar activity.

The bubble distribution was investigated by C/NOFS during solar minimum, and the bubble was seen after midnight in northern summer (Huang et al., 2014). In Figure 6, BPD is well observed at longitude of 0 degree-90 degrees, and according to Huang et al. (2014), bubbles are observed in similar regions. The longitudinal distribution of the BPD is consistent with the distribution of longitude of relative density perturbations as well as plasma density perturbations. However, the number of BPD encounters has a secondary peak in 240 degrees-360 degrees and a minimum in 90 degrees-240 degrees. However, the bubble does not follow the longitudinal distribution of BPDs. That is, the bubble does not show the secondary peak and minimum longitudes. Ionospheric uplift can be favorable to the generation of both bubbles and BPDs, which may be responsible for their common occurrence peaks at longitude of 0 degree-90

degrees. However, the longitudinal distributions of BPD and bubble do not completely match, so the mechanism of BPD generation cannot be solely explained by the merging process suggested by Huang et al. (2011).

Recently, plasma bubbles have been reported over a wide latitude range in the ionosphere – for example, super plasma bubbles. With storm and concomitant prompt penetration electric field, plasma bubbles occurred in westward Africa and extended to European middle latitude (30°-40°N) (Cherniak et al., 2016). Analysis of Millstone Incoherent scatter radar and GNSS TEC data for geomagnetic storms showed that a strong equatorial plasma bubble was grown and combined with mesoscale traveling ionospheric disturbances (Aa et al., 2019). These super plasma bubbles seemed to span a wide latitude range, just as equatorial BPDs have a large longitudinal extent. The relationship between BPDs and super plasma bubbles is an interesting topic, which has been left for future study.

4.2. Premidinght BPDs during moderate solar activity

Although the occurrence rate is low, premidnight BPDs occur mainly during relatively high solar activity. During this period, the equatorial ionosphere does not necessarily have a lower scale height and weakly downward plasma drift: it is not a good environment for the occurrence of BPDs. Premidnight BPDs are observed with high Kp indices, which signifies strong storms. If an exceptionally strong eastward electric field is induced in the pre-midnight equatorial ionosphere by the prompt penetration electric field effect, the F region uplift can become stronger even though the background electric field is directed westward. The requirement for exceptional strength of eastward E-field may explain the low occurrence of pre-midnight BPDs during relatively higher solar activity in comparison to that of post-midnight BPDs during solar

minimum years. Considering the statistical properties of the two groups of BPDs divided by local time, the BPDs occurrences depend strongly on local time and solar activity. When the lower scale height and stagnant background make favorable environments for BPD generation during solar minimum, the storm-time disturbance dynamo can easily trigger the uplift of the equatorial ionosphere and generate prominent BPDs. It was considered as BPDs when satellite pass through the larger structure of plasma density depletion.

5. Conclusions

We have investigated the statistical distribution in the occurrence of BPDs using the plasma density data measured by the PLP instrument on board the C/NOFS satellite in 2008-2012. We have also developed a code to find BPDs automatically.

Although premidnight BPDs have been found in previous studies, BPDs are mainly observed at lower apex height at postmidnight. BPDs were also frequently observed in the June solstice of low solar activity. The tendency of the BPD occurrence rate was similar to that of the AE index, and showed a clear inverse correlation with the 10.7 cm solar radio flux.

Why are BPDs often observed in postmidnight, solar minimum, and June solstice? The reason why BPD is frequently observed in low solar activity periods is because lower scale height and stagnant post-midnight background plasma forms a favorable environment for the production of BPDs. Under this pre-condition, storm-time disturbance dynamo can easily generate post-midnight BPDs. Even if the F region rises slightly due to the disturbance-induced electric field, the satellites can pass through the bottomside plasma more easily than for high solar activity.

Since the F region is thick in high solar activity, a strong disturbance-induced electric field in support of eastward background field (e.g., pre-reversal enhancement) is necessary in order for the F region to be raised to create the BPD at satellite altitudes. Therefore, we suggest that BPDs in high solar activity are observed only if a strong prompt penetration electric field is superposed to pre-reversal enhancement in premidnight. A satellite at lower apex altitudes has a higher chance of detecting BPD.

Acknowledgements

This research was supported by basic research funding from Korea Astronomy and Space Science Institute (KASI). J.-M. Choi was also supported by the Ministry of Science and Technology, Taiwan (MOST) under project MOST 108-2638-M-006-001-MY2. Part of the work is supported by National Space Organization, Taiwan (NSPO) under project NSPO-S-109065. The C/NOFS data are available in the NASA database (http://cdaweb.gsfc.nasa.gov/istp_public/). The Jicamarca ISR data for this paper were obtained from the CEDAR Madrigal Database at http://cedar.openmadrigal.org. The OMNI data were obtained from the GSFC/SPDF OMNIWeb interface at https://omniweb.gsfc.nasa.gov.

References

Aa, E., Zou, S., Ridley, A. J., Zhang, S.-R., Coster, A. J., Erickson, P. J., et al. (2019). Merging of storm time mid-latitude traveling ionospheric disturbances and equatorial plasma bubbles. *Space Weather, 17,* 285– 298. https://doi.org/10.1029/2018SW002101

Abdu, M. A., Bittencourt, J. A., & Batista, I. S. (1981). Magnetic declination control of the equatorial *F* region dynamo electric field development and spread *F*. *Journal of Geophysical Research, 86,* 11,443–11,446. https://doi.org/10.1029/JA086iA13p11443

Abdu, M. A., Batista, I. S., & Sobral, J. (1992). A new aspect of magnetic declination control of equatorial spread *F* and *F* region dynamo. *Journal of Geophysical Research, 97(A10),* 14,897–14,904. https://doi.org/10.1029/92JA00826

Abdu, M. A., Kherani, E. A., Batista, I. S., & Sobral, J. H. A. (2009). Equatorial evening prereversal vertical drift and spread *F* suppression by disturbance penetration electric fields. *Geophysical Research Letter, 36,* L19103. https://doi.org/10.1029/2009GL039919

Basu, S., Basu, S., Rich, F. J., Groves, K. M., MacKenzie, E., Coker, C., Sahai, Y., Fagundes, P. R., & Becker-Guedes, F. (2007). Response of the equatorial ionosphere at dusk to penetration electric fields during intense magnetic storms. *Journal of Geophysical Research, 112,* A08308. https://doi.org/10.1029/2006JA012192

Blanc, M., & Richmond, A. (1980). The ionospheric disturbance dynamo. *Journal of Geophysical Research, 85(A4)*, 1669– 1686. https://doi.org/10.1029/JA085iA04p01669

Burke, W. J., Rubin, A. G., Maynard, N. C., Gentile, L. C., Sultan, P. J., Rich, F. J., de La Beaujardière, O., Huang, C. Y., & Wilson, G. R. (2000). Ionospheric disturbances observed by DMSP at middle to low latitudes during the magnetic storm of June 4–6, 1991. *Journal of Geophysical Research, 105(A8)*, 18,391–18,405. https://doi.org/10.1029/1999JA000188

Burke, W. J., de La Beaujardière, O., Gentile, L. C., Hunton, D. E., Pfaff, R. F., Roddy, P. A., Su, Y.-J., & Wilson, G. R. (2009). C/NOFS observations of plasma density and electric field irregularities at post-midnight local times. *Geophysical Research Letter, 36*, L00C09. https://doi.org/10.1029/2009GL038879

Cherniak, I., & Zakharenkova, I. (2016). First observations of super plasma bubbles in Europe. *Geophysical Research Letter, 43*, 11,137– 11,145. https://doi.org/10.1002/2016GL071421

Fejer, B. G., dePaula, E. R., Gonzalez, S. A., & Woodman, R. F. (1991). Average vertical and zonal F region plasma drifts over Jicamarca. *Journal of Geophysical Research, 96(A8)*, 13,901–13,906. https://doi.org/10.1029/91JA01171

Fejer, B. G., dePaula, E. R., Heelis, R. A., & Hanson, W. B. (1995). Global equatorial ionospheric vertical plasma drifts measured by the AE-E satellite. *Journal of Geophysical Research, 100*, 5769–5776. https://doi.org/10.1029/94JA03240

Greenspan, M. E., Rasmussen, C. E., Burke, W. J., & Abdu, M. A. (1991). Equatorial density depletions observed at 840 km during the greatmagnetic storm of March 1989. *Journal of Geophysical Research, 96(A8)*, 13,931–13,942. https://doi.org/10.1029/91JA01264

Hargreaves, J. K. (1992). The Solar-Terrestrial Environment, 218 pp., Cambridge Univ. Press, Cambridge, U. K.

Huang, C.-S., de La Beaujardière, O., Roddy, P. A., Hunton, D. E., Pfaff, R. F., Valladares, C. E., & Ballenthin, J. O. (2011). Evolution of equatorialionospheric plasma bubbles and formation of BPDs measured by the C/NOFS satellite during deep solar minimum. *Journal of Geophysical Research*, *116*, A03309. https://doi.org/10.1029/2010JA015982

Huang, C.-S., Retterer, J. M., de La Beaujardière, O., Roddy, P. A., Hunton, D. E., Ballenthin, J. O., & Pfaff, R. F. (2012). Observations and simulations of formation of broad plasma depletions through merging process. *Journal of Geophysical Research*, *117*, A02314. https://doi.org/10.1029/2011JA017084

Huang, C.-S., La Beaujardiere, O., Roddy, P. A., Hunton, D. E., Liu, J. Y., and Chen, S. P. (2014). Occurrence probability and amplitude of equatorial ionospheric irregularities associated with plasma bubbles during low and moderate solar activities (2008–2012). *Journal of Geophysical Research: Space Physics*, *119*, 1186– 1199. https://doi.org/10.1002/2013JA019212

Huang, C. Y., Marcos, F. A., Roddy, P. A., Hairston, M. R., Coley, W. R., Roth, C., Bruinsma, S., and Hunton, D. E. (2009). Broad plasma decreases in the equatorial ionosphere. *Geophysical Research Letter*, *36*, L00C04. https://doi.org/10.1029/2009GL039423

Kil, H., & Paxton, L. J. (2006). Ionospheric disturbances during the magnetic storm of 15 July 2000: Role of the fountain effect and plasma bubbles for the formation of large equatorial plasma density depletions. *Journal of Geophysical Research, 111*, A12311. https://doi.org/10.1029/2006JA011742

Kil, H., Paxton, L. J., Su, S.-Y., Zhang, Y., & Yeh, H. (2006). Characteristics of the storm-induced big bubbles (SIBBs). *Journal of Geophysical Research, 111*, A10308. https://doi.org/10.1029/2006JA011743

Kil, H., & Lee, W. K. (2013). Are plasma bubbles a prerequisite for the formation of broad plasma depletions in the equatorial F region?. *Geophysical Research Letter*, *40*, 3491–3495. https://doi.org/10.1002/grl.50693

Kil, H., Kwak, Y.-S., Lee, W. K., Oh, S.-J., Milla, M., & Galkin, I. (2014). Broad plasma depletions detected in the bottomside of the equatorial F region: Simultaneous ROCSAT-1 and JULIA observations, *Journal of Geophysical Research: Space Physics*, *119*, 5978–5984. https://doi.org/10.1002/2014JA019964

426 Kil, H., Lee, W. K., Paxton, L. J., Hairston, M. R., & Jee, G. (2016). Equatorial broad plasma
427 depletions associated with the evening prereversal enhancement and plasma bubbles during the
428 17 March 2015 storm. *Journal of Geophysical Research: Space Physics*, *121*, 10,209–10,219.
429 https://doi.org/10.1002/2016JA023335
430
431 Lee, J. J., Min, K. W., Kim, V. P., Hegai, V. V., Oyama, K.-I., Rich, F. J., & Kim, J. (2002).
432 Large density depletions in the nighttime upper ionosphereduring the magnetic storm of July 15,
433 2000. *Geophysical Research Letter*, *29(3)*,1032. https://doi.org/10.1029/2001GL013991
434
435 Lee, W. K., Kil, H., Kwak, Y.-S., Paxton, L. J., Zhang, Y., Galkin, I., & Batista, I. S. (2014).
436 Equatorial broad plasma depletions associated with the enhanced fountain effect. *Journal of*
437 *Geophysical Research*, *119*, 402–410. https://doi.org/10.1002/2013JA019137
438
439 Lee, C.-C., & Reinisch, B. W. (2007). Quiet-condition variations in thescale height at F2-layer
440 peak at Jicamarca during solar minimum and maximum. *Annales Geophysicae*, 25(12), 2541–
441 2550. https://doi.org/10.5194/angeo-25-2541-2007
442
443 Liu, L., Wan, W., & Ning, B. (2006). A study of the ionogram derived effectivescale height
444 around the ionospheric hmF2. *Annales Geophysicae*, *24(3)*, 851–860.
445 https://doi.org/10.5194/angeo-24-851-2006
446

Liu, L., Yang, J., Le, H., Chen, Y., Wan, W., & Lee, C.-C. (2012). Comparative study of the equatorial ionosphere over Jicamarca during recent two solar minima. *Journal of Geophysical Research*, *117*, A01315, https://doi.org/10.1029/2011JA017215

Nishioka, M., Otsuka, Y., Shiokawa, K., Tsugawa, T., Effendy, Supnithi, P., Nagatsuma, T., & Murata, K. T. (2012). On post-midnight field-aligned irregularities observed with a 30.8-MHz radar at a low latitude: Comparison with F-layer altitude near the geomagnetic equator. *Journal of Geophysical Research*, *117*, A08337, https://doi.org/10.1029/2012JA017692

Su, S.-Y., Yeh, H. C., Chao, C. K., & Heelis, R. A. (2002). Observation of a large density dropout across the magnetic field at 600 km altitude duringthe 6–7 April 2000 magnetic storm. *Journal of Geophysical Research*, *107(A11)*, 1404, https://doi.org/10.1029/2001JA007552

Smith, J. M., & Heelis, R. A. (2018). The plasma environment associated with equatorial ionospheric irregularities. *Journal of Geophysical Research: Space Physics*, *123*, 1583– 1592. https://doi.org/10.1002/2017JA024933

Stoneback, R. A., Heelis, R. A., Burrell, A. G., Coley, W. R., Fejer, B. G., & Pacheco, E. (2011). Observations of quiet time vertical ion drift in the equatorial ionosphere during the solar minimum period of 2009. *Journal of Geophysical Research*, *116*, A12327. https://doi.org/10.1029/2011JA016712

Yokoyama, T., Shinagawa, H., & Jin, H. (2014). Nonlinear growth, bifurcation and pinching of equatorial plasma bubble simulated by three-dimensional high-resolution bubble model. *Journal of Geophysical Research: Space Physics*, *119*, 10,474–10,482. https://doi.org/10.1002/2014JA020708

Figure captions

Figure 1. Examples of automatic BPDs search process in the C/NOFS satellite data. (a) In-situ measurements of plasma density. The red solid line represents the background density. (b) The difference between the logarithm of the plasma density and logarithm of the background density. (c) The absolute values of the results in Figure 1b. The red dashed line represents the threshold value. (d) Results considered the threshold value. (e) The final processed BPDs.

Figure 2. Statistical distribution of the occurrence of BPDs as a function of (a) local time, (b) magnetic latitude, (c) the Kp index, and (d) apex altitude, when BPDs were automatically searched in the C/NOFS data from June 2008 to December 2012. Blue and green bars indicate the occurrence rates of the postmidnight PBDs and the premidnight BPDs, respectively.

Figure 3. Monthly distribution of occurrence rate of BPDs observed by C/NOFS satellite during 2008-2012. The blue lines show the AE index.

Figure 4. Seasonal variation of BPDs in (a) June solstice, (b) December solstice, (c) equinox. The red lines indicate the 10.7 cm solar radio flux.

Figure 5. Median vertical plasma drifts over Jicamarca during June solstice (May, June, July, and August), December solstice (November, December, January, and February), and equinox (March, April, September, and October) for solar minimum and moderate flux conditions. The error bars denote upper and lower quartile of the median values. The left and right panel indicate median vertical plasma drift in solar minimum (2008-2009) and solar moderate (2011-2012), respectively. The number of data points is given at the top of each panel.

Figure 6. Longitudinal variation of BPDs.

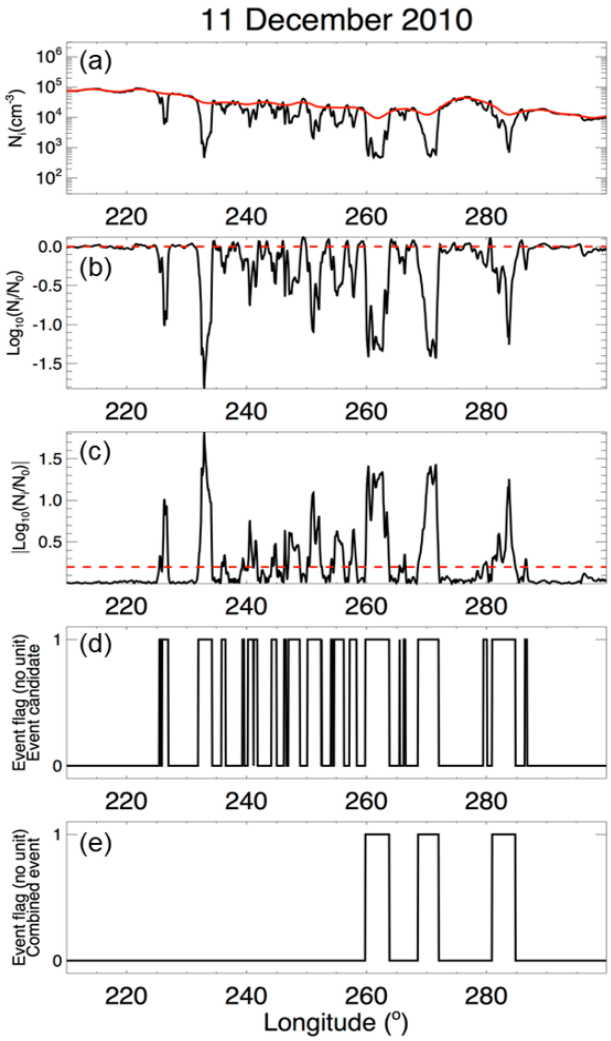

519

520 **Figure 1.** Examples of automatic BPDs search process in the C/NOFS satellite data. (a) In-situ
521 measurements of plasma density. The red solid line represents the background density. (b) The
522 difference between the logarithm of the plasma density and logarithm of the background density.
523 (c) The absolute values of the results in Figure 1b. The red dashed line represents the threshold
524 value. (d) Results considered the threshold value. (e) The final processed BPDs.

525

526

527

528

529

530

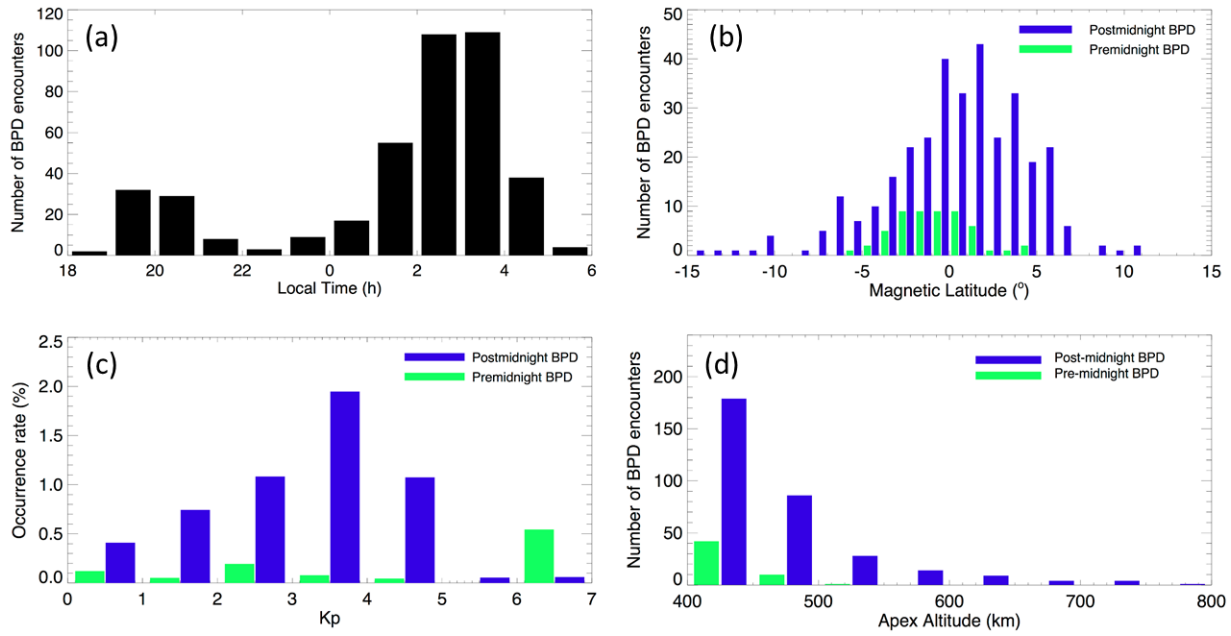

Figure 2. Statistical distribution of the occurrence of BPDs as a function of (a) local time, (b) magnetic latitude, (c) the Kp index, and (d) apex altitude, when BPDs were automatically searched in the C/NOFS data from June 2008 to December 2012. Blue and green bars indicate the occurrence rates of the postmidnight PBDs and the premidnight BPDs, respectively.

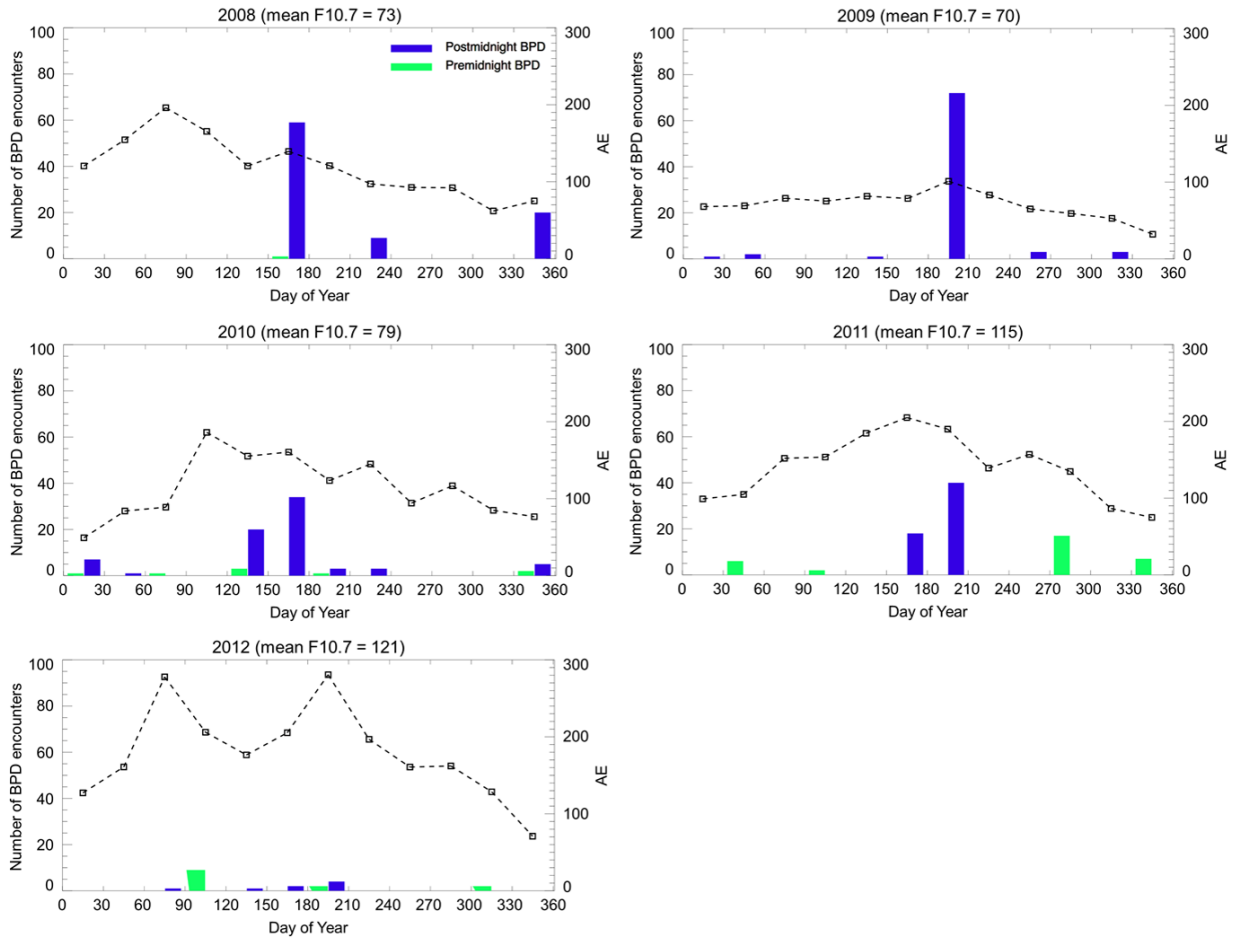

547

548 **Figure 3.** Monthly distribution of occurrence rate of BPDs observed by C/NOFS satellite during
549 2008-2012. The black dashed lines show the AE index.

550

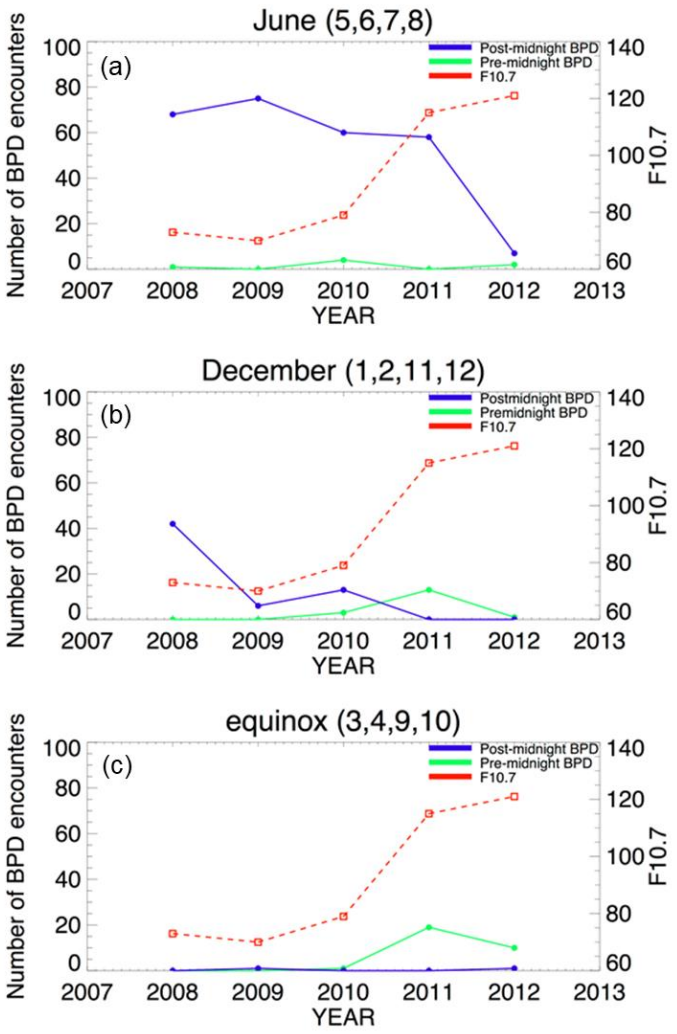

551

552 **Figure 4.** Year-to-year variation of BPDs in (a) June solstice, (b) December solstice, (c) equinox.
553 The red dashed lines indicate the 10.7 cm solar radio flux.

554

555

556

557

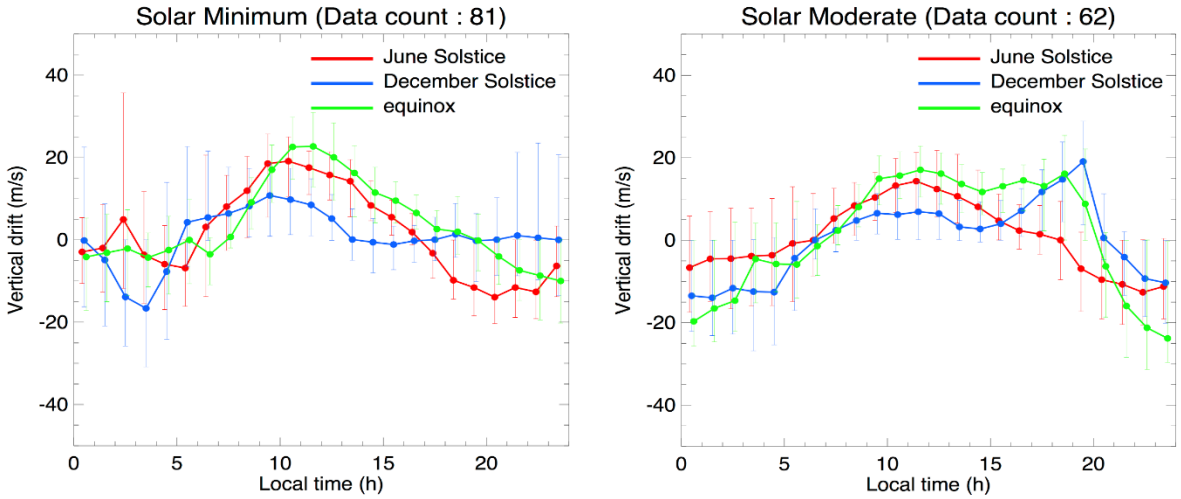

Figure 5. Median vertical plasma drifts over Jicamarca during June solstice (May, June, July, and August), December solstice (November, December, January, and February), and equinox (March, April, September, and October) for solar minimum and moderate flux conditions. The error bars denote upper and lower quartile of the median values. The left and right panel indicate median vertical plasma drift in solar minimum (2008-2009) and solar moderate (2011-2012), respectively. The number of data points is given at the top of each panel.

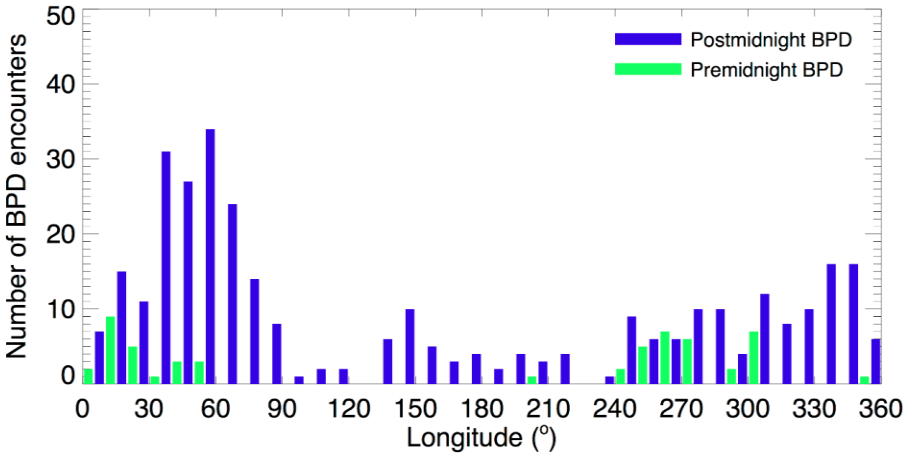

574

575 **Figure 6.** Longitudinal variation of BPDs.

576

577

578

579

580

581

582

Figure 1.

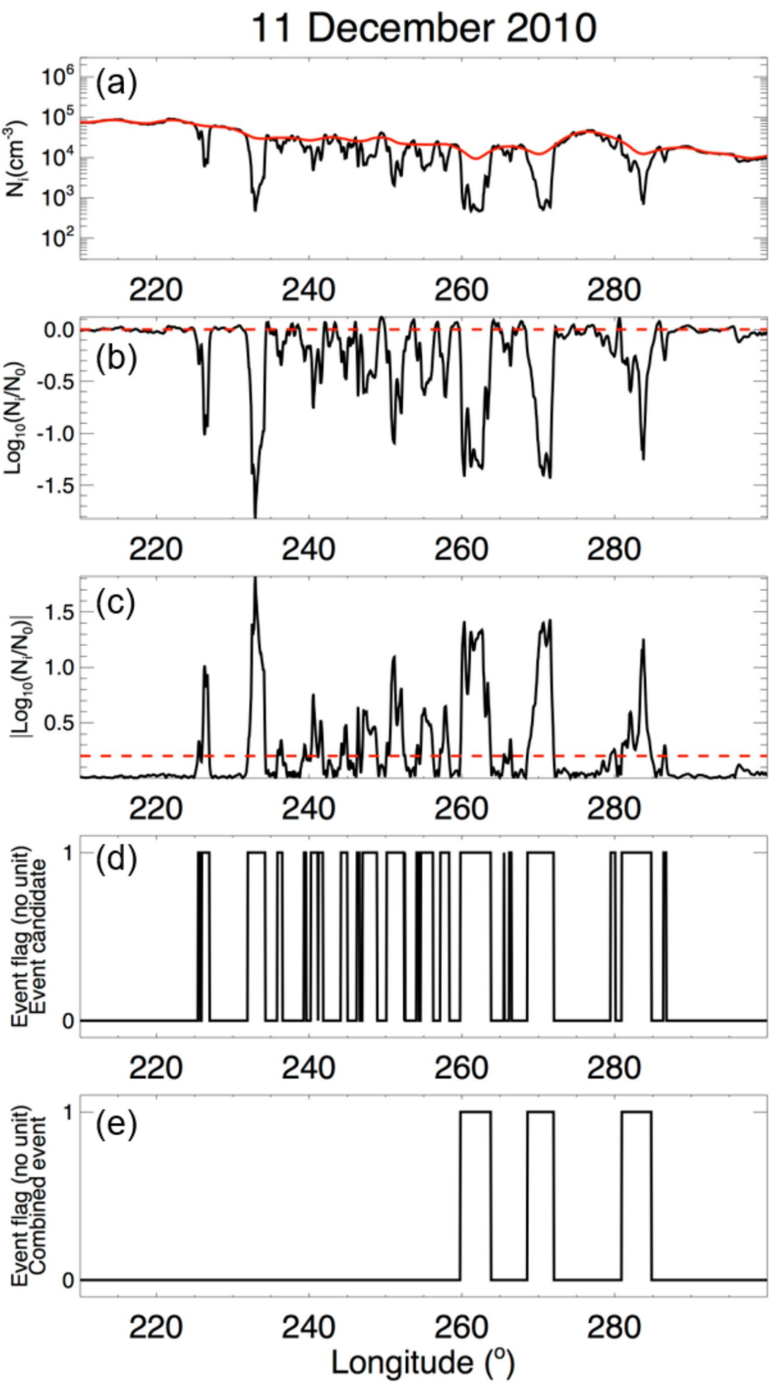
11 December 2010
(a)
$N_i(cm^{-3})$
10^6
10^5
10^4
10^3
10^2
220
240
260
280
(b)
$Log_{10}(N_i/N_0)$
0.0
-0.5
-1.0
-1.5
220
240
260
280
(c)
$|Log_{10}(N_i/N_0)|$
1.5
1.0
0.5
220
240
260
280
(d)
Event flag (no unit)
Event candidate
1
0
220
240
260
280
(e)
Event flag (no unit)
Combined event
1
0
220
240
260
280
Longitude (°)

Figure 2.

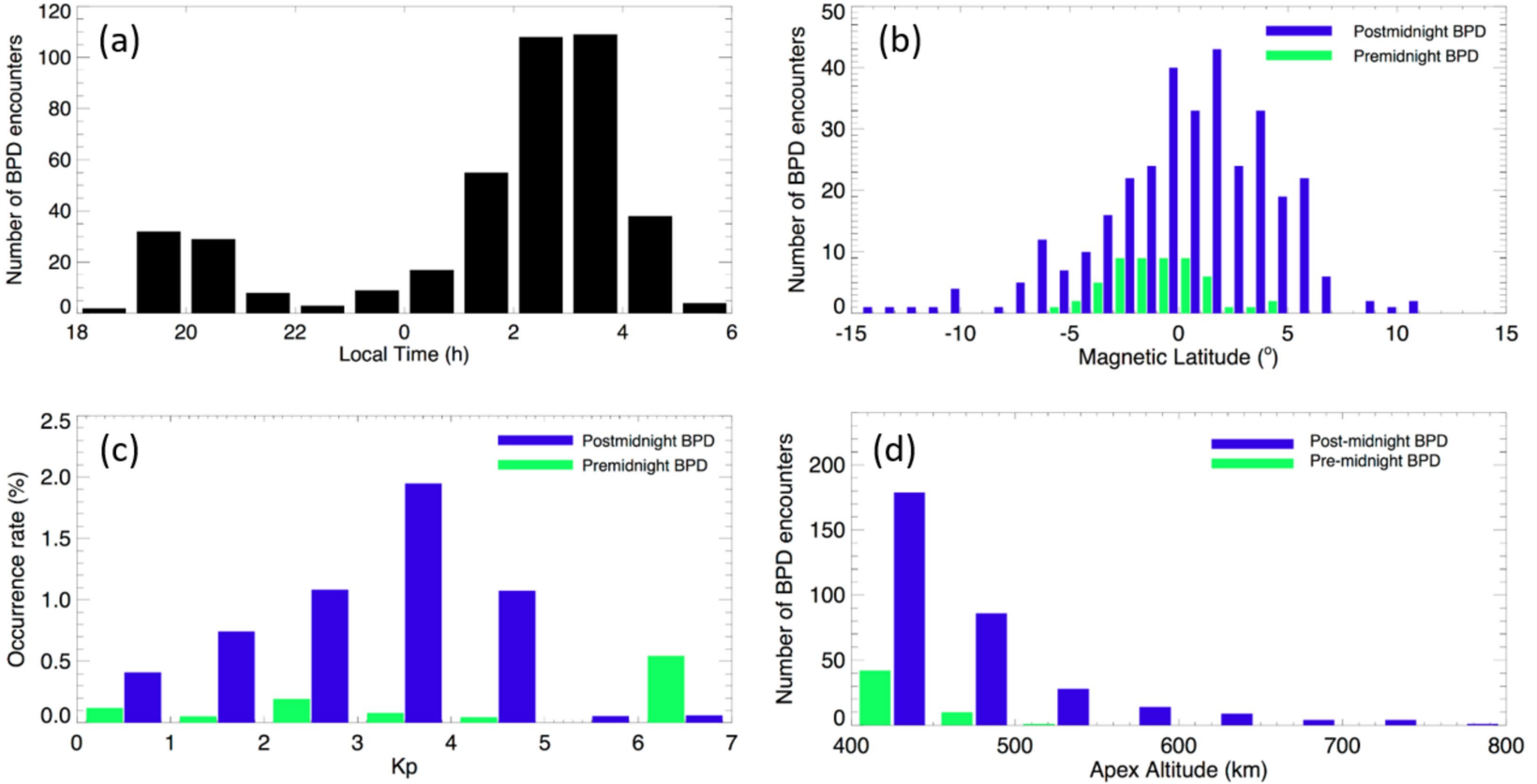
(a)
Number of BPD encounters
Local Time (h)
(b)
Postmidnight BPD
Premidnight BPD
Number of BPD encounters
Magnetic Latitude (°)
(c)
Postmidnight BPD
Premidnight BPD
Occurrence rate (%)
Kp
(d)
Post-midnight BPD
Pre-midnight BPD
Number of BPD encounters
Apex Altitude (km)

Figure 3.

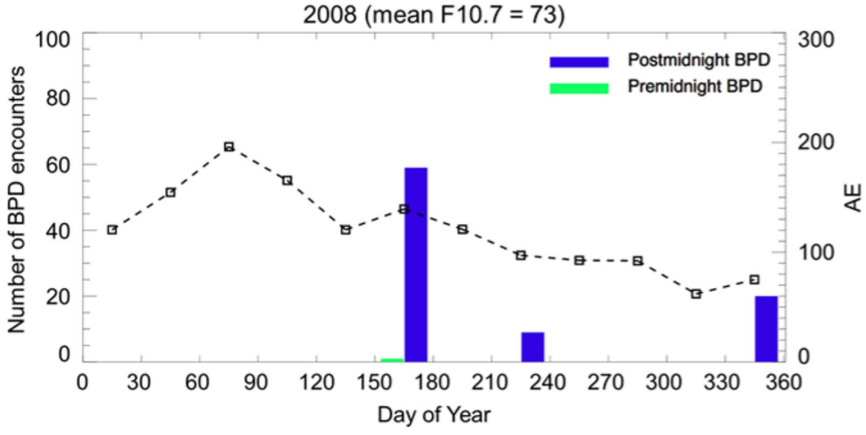
2008 (mean F10.7 = 73)
Postmidnight BPD
Premidnight BPD
Number of BPD encounters
AE
Day of Year

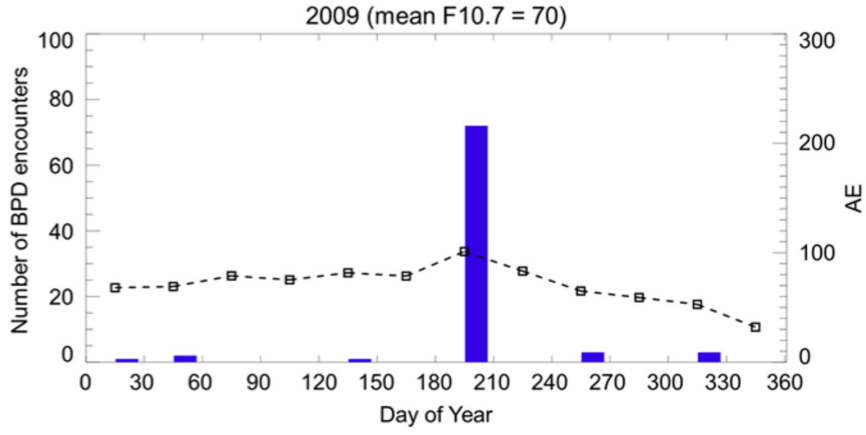
2009 (mean F10.7 = 70)
Number of BPD encounters
AE
Day of Year

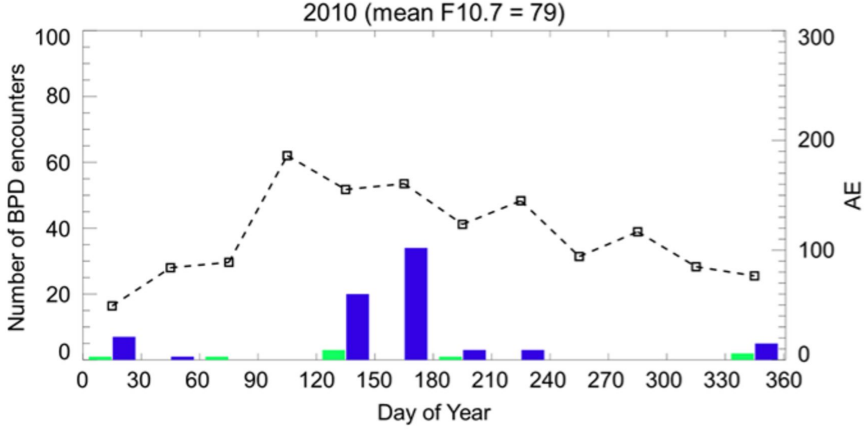
2010 (mean F10.7 = 79)
Number of BPD encounters
AE
Day of Year

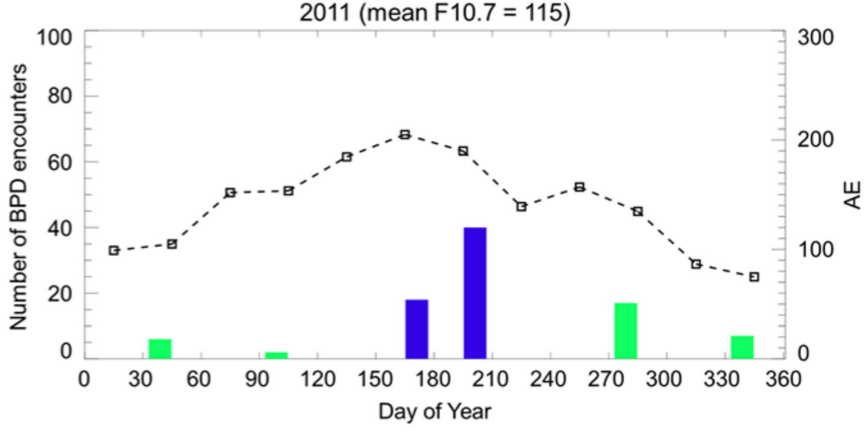
2011 (mean F10.7 = 115)
Number of BPD encounters
AE
Day of Year

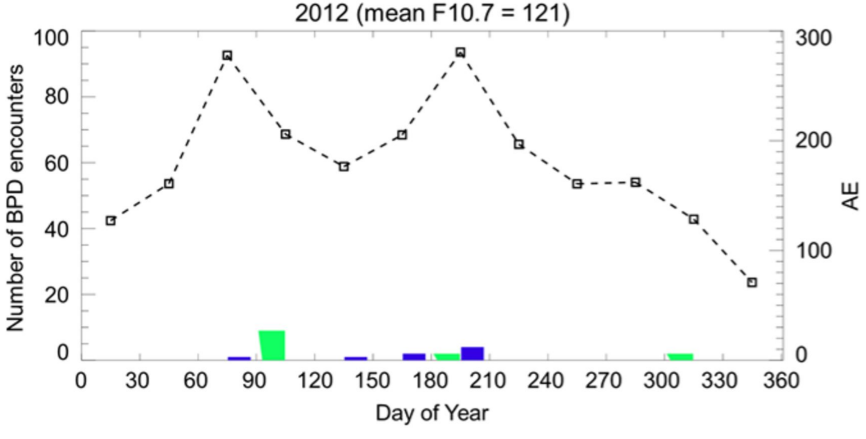
2012 (mean F10.7 = 121)
Number of BPD encounters
AE
Day of Year

Figure 4.

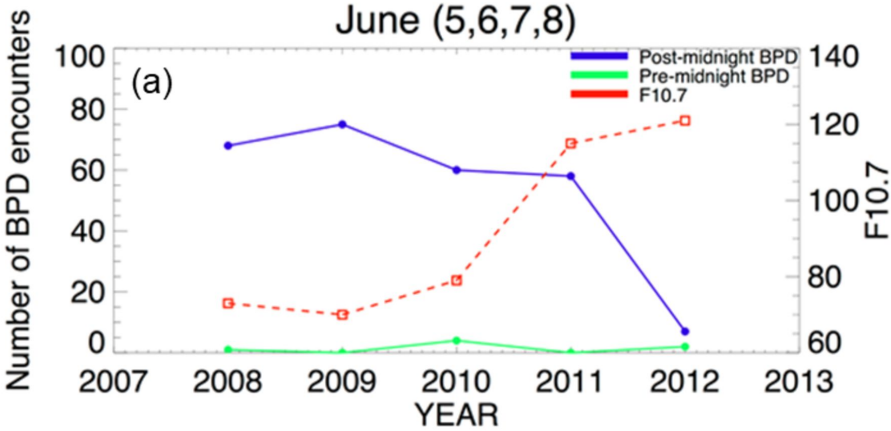
June (5,6,7,8)
(a)
Post-midnight BPD
Pre-midnight BPD
F10.7
Number of BPD encounters
F10.7
YEAR
100
80
60
40
20
0
140
120
100
80
60
2007
2008
2009
2010
2011
2012
2013

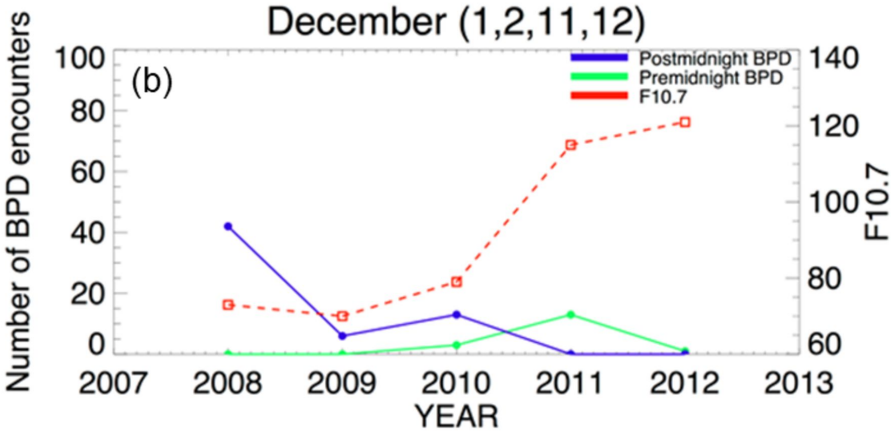
December (1,2,11,12)
(b)
Postmidnight BPD
Premidnight BPD
F10.7
Number of BPD encounters
F10.7
YEAR
100
80
60
40
20
0
140
120
100
80
60
2007
2008
2009
2010
2011
2012
2013

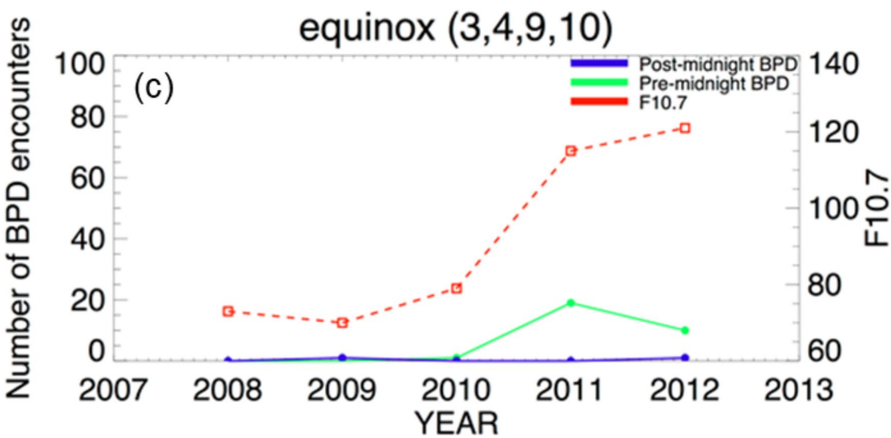
equinox (3,4,9,10)
(c)
Post-midnight BPD
Pre-midnight BPD
F10.7
Number of BPD encounters
F10.7
YEAR
100
80
60
40
20
0
140
120
100
80
60
2007
2008
2009
2010
2011
2012
2013

Figure 5.

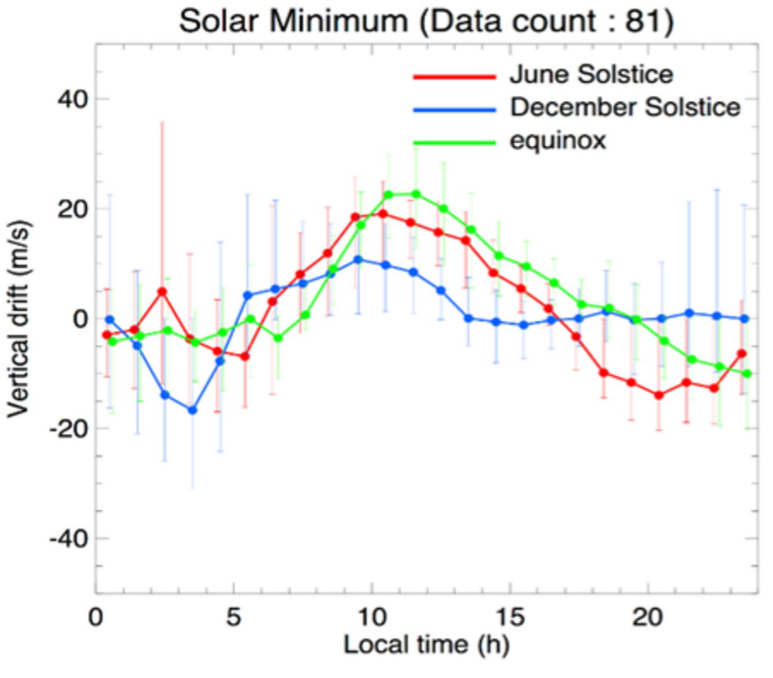
Solar Minimum (Data count : 81)
June Solstice
December Solstice
equinox
Vertical drift (m/s)
40
20
0
-20
-40
0
5
10
15
20
Local time (h)

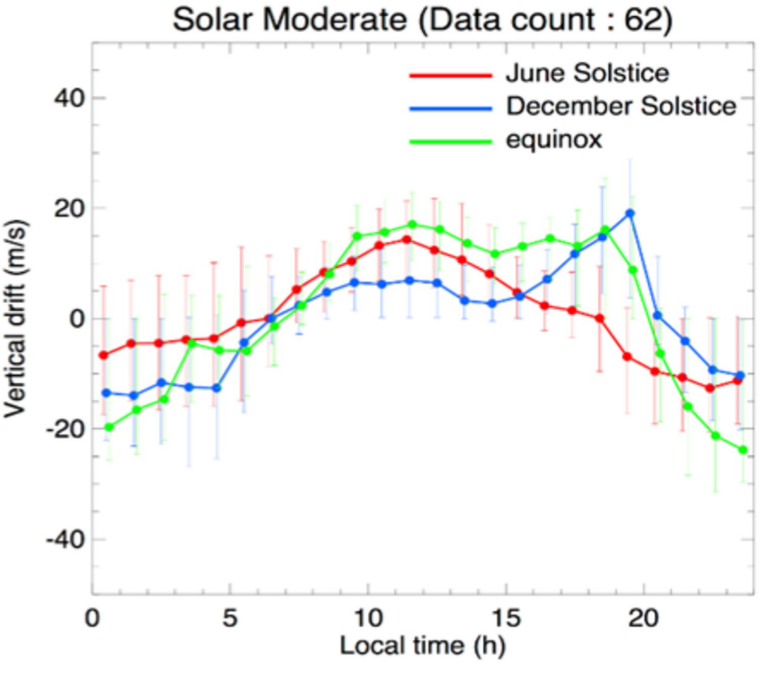
Solar Moderate (Data count : 62)
June Solstice
December Solstice
equinox
Vertical drift (m/s)
40
20
0
-20
-40
0
5
10
15
20
Local time (h)

Figure 6.

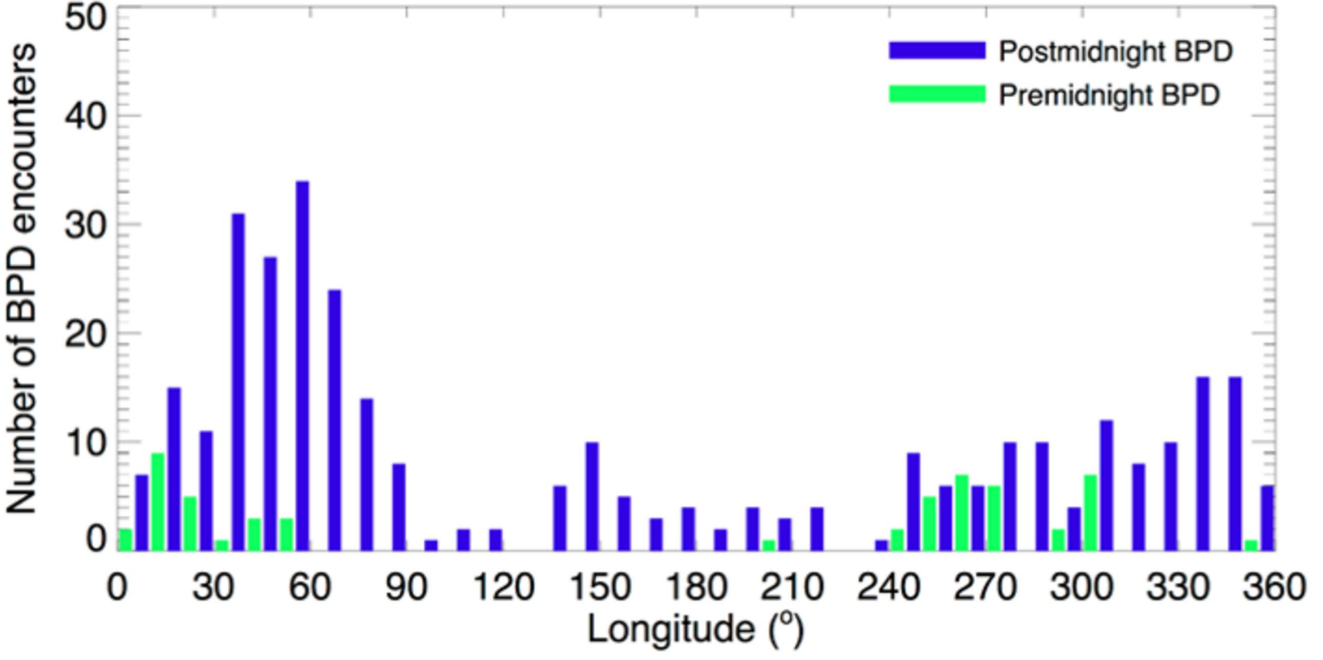
Postmidnight BPD
Premidnight BPD
Number of BPD encounters
0
10
20
30
40
50
0
30
60
90
120
150
180
210
240
270
300
330
360
Longitude (°)